

DYNAMICS OF BOTTOM TRAPPED CURRENTS WITH APPLICATION TO THE STRAIT OF GEORGIA

MATEUSZ K. RESZKA AND GORDON E. SWATERS

ABSTRACT. We present a numerical study of bottom-trapped, density-driven flows using a frontal geostrophic model in which the ambient ocean is continuously stratified. The model focuses on the release of gravitational potential energy associated with the descent of a gravity current down an incline in a rotating reference frame. In the resulting system, the overlying fluid is stratified and quasigeostrophic, while the deep current is homogeneous and the interface is allowed to intersect the oceanic bottom. We show that such currents preferentially develop plumes on the downslope side, which rapidly roll up into more coherent features. In response to deformations of the interface, eddies emerge in the overlying fluid and extend over most of the fluid column but are bottom-intensified with a tapered vertical structure. These results are in good agreement with observations in the Strait of Georgia, where dense water intrusions are known to produce tapered eddies a few kilometers in diameter. Based on our findings, we conclude that continuous upper layer stratification is an important aspect of this dynamical regime.

1. Introduction. Density-driven benthic flows occur throughout the world's oceans. They are most often associated with sloping continental shelves but can also be found along mid-ocean ridges and canyons. For example, North Atlantic Deep Water and Antarctic Bottom Water form in polar regions and subsequently travel equatorward as concentrated, topographically-steered benthic currents (Haine et al. [11], Rahmstorf [27]). In the global sense, bottom-trapped currents play an integral role in thermohaline circulation and are a vehicle for the transport of heat, salt, oxygen and nutrients over great distances. The ability of abyssal flows to transport and deposit sediment is also of geological interest (Smith [32]). The migration and evolution of dense water masses are important in the dynamics of marginal seas, river estuaries and other coastal regions (Price and O'Neil Baringer [26]). A number of studies have noted the annual formation of a cold pool in the Middle Atlantic Bight, (e.g. Houghton et al. [12]), as well as episodic intrusions of deep water along the coast of British Columbia, Canada

(LeBlond et al. [21]). There is mounting evidence that such flows are subject to instability, which may drastically alter the mean flow and culminate in a series of isolated plumes or eddies (Houghton et al. [12], Armi and D'Asaro [2]).

A detailed, as well as intriguing, data set was obtained by Stacey et al. [35] regarding the low-frequency dynamics of a dense, bottom-trapped current in the Strait of Georgia, (henceforth SOG), a semi-enclosed basin between Vancouver Island and mainland British Columbia. This survey employed an array of cyclosonde and current-meter moorings which gathered data from June, 1984 to January, 1985 in one region of the strait. The moorings were placed close enough together that small scale features on the order of a few kilometers could be resolved. Subsequent analyses (Stacey et al. [36], [37]) revealed highly nonlinear flowfields with relatively short time scales. There was clear evidence of bottom-intensified cyclonic and anticyclonic eddies, with length scales on the order of 10 km. It was suggested that the high degree of spatial and temporal variability within the strait was, at least sometimes, the result of baroclinic instability.

Early modeling efforts aimed at the description of deep water transport included Smith [32] and Killworth [19], who employed the steady streamtube approximation. A linear instability calculation in the context of reduced gravity shallow water equations was performed by Griffiths et al. [10]; however, this analysis naturally precluded the existence of baroclinic motions. Further theoretical studies of density-driven gravity currents were also conducted by, for example, Speer et al. [34] as well as Shapiro and Hill [31]. Because they exist at great depths, often in the inhospitable high latitudes, deep water masses are difficult to observe directly, and much of our understanding about their variability comes from numerical and laboratory investigations. For example, Gawarkiewicz and Chapman [9] studied the offshore transport of dense water in an Arctic polynya, while Jiang and Garwood Jr. [14] analyzed the behavior of the Denmark Strait Overflow. The breakup of a bottom-trapped jet into distinct baroclinic eddies was studied experimentally by Whitehead et al. [41], among others.

Mesoscale gravity currents, which are to be discussed in this study, arise from a geostrophic balance between down-slope acceleration due to gravity and the Coriolis force, while their dynamics is characterized by lengthscales on the order of the Rossby deformation radius. They are

thus markedly different from smaller-scale gravity currents which are relatively unaffected by rotation (see, for example, Britter and Linden [4]). In accordance with the sign of the Coriolis parameter, mesoscale gravity currents tend to flow along bathymetric contours with shallower water on their right in the northern hemisphere and their left in the southern hemisphere. Swaters [38] developed a non-quasigeostrophic model in which the subinertial baroclinic dynamics of mesoscale gravity currents is modeled as a balance between relative vorticity production and vortex-tube stretching/compression associated with a deforming gravity current height in the presence of a background topographic potential vorticity gradient. This two-layer frontal-geostrophic theory was subsequently employed in a linear instability calculation appropriate for the SOG by Karsten et al. [15]. Their analysis predicted instability with quick growth rates; however, the wavelength of the dominant mode was about twice that needed to explain the observed eddies.

Poulin and Swaters [24] and [25] presented a more general frontal geostrophic model which provides an improved description of the vertical structure of the fluid column by allowing for continuous stratification in the upper layer. In the case of a wedge front basic state, the dominant length scales associated with this model were shown to be smaller than those obtained for the Swaters [38] theory. Moreover, the continuously stratified model has the potential to reproduce the bottom-intensified nature of eddies observed in the SOG. In this work, we present numerical simulations of deep water evolution using both models and compare our results with the Stacey et al. [35], [36] observational record. In particular, it is shown that the emerging lengthscales, as well as the eddy vertical structure, are in agreement with the observations in the SOG.

It must be noted that several other research efforts have focused on modeling SOG dynamics in recent years. A comprehensive numerical study of deep water processes was carried out by Marinone and Pond [22] (see also references therein), which captured tides and residual currents in the SOG quite well. While the coarse resolution of their 3D primitive equation model (2 km in the horizontal, 8 layers in the vertical) gave a poor representation of small scale fluctuations and vortices, it is likely that this obstacle can be overcome with improved computational resources. In the present investigation, however, the approach is somewhat different. Rather than obtaining a complete

description of the estuarine circulation, our aim is to focus on baroclinic instability in a simple channel domain, in order to better understand this aspect of low-frequency variability in the SOG. Having reduced the problem to its essentials, the results could, in principle, be applied to similar oceanographic settings of interest, such as the Denmark Strait Overflow (see for example Bruce [5]).

The outline of the paper is as follows: In Section 2, we briefly describe the derivation of both models and give details concerning our computational technique. Section 3 deals with analytical and numerical results for a simple, highly idealized flow without incroppings, i.e., a wedge front. Simulations pertaining to the SOG are presented in Section 4. Section 5 contains a closer analysis of the instability mechanism, while concluding remarks and potential avenues for further research are given in Section 6.

2. Governing equations. The present model assumes a continuously stratified layer of finite depth overlying a dense, homogeneous layer and sloping (or otherwise varying) bottom topography. The interface between the two layers can intersect the topography (see Figure 1), allowing for isolated patches of dense fluid. The governing equations are derived in an asymptotic expansion of the shallow water equations for the lower layer and the Boussinesq equations for the upper layer. We refer the reader to Poulin and Swaters [24] for details. The leading order nondimensional equations on a β -plane are given by

$$(2.1) \quad (\Delta\varphi + (N^{-2}\varphi_z)_z)_t + \mu J(\varphi, \Delta\varphi + (N^{-2}\varphi_z)_z + \beta y) = 0,$$

together with the time-dependent vertical boundary conditions

$$(2.2) \quad \varphi_{zt} + \mu J(\varphi, \varphi_z) = 0, \quad z = 0,$$

$$(2.3) \quad \varphi_{zt} + \mu J(\varphi, \varphi_z) + N^2 J(\varphi + h, h_B) = 0, \quad z = -1,$$

$$(2.4) \quad h_t + J(\mu\varphi + h_B, h) = 0, \quad z = -1,$$

where $\varphi(x, y, z, t)$ is the upper layer geostrophic pressure, $h(x, y, t)$ is the lower layer thickness, $h_B(x, y)$ is the height of the bottom topography, $J(A, B) = A_x B_y - B_x A_y$ and subscripts refer to derivatives unless otherwise specified. Here N^2 is equivalent to the Burger number associated with the upper layer and μ is referred to as the interaction

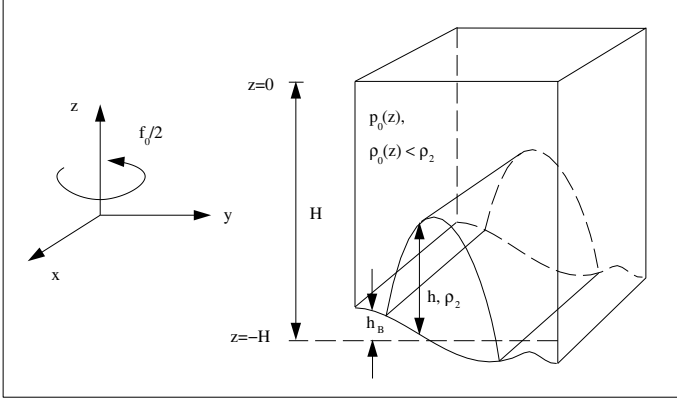


FIGURE 1. Geometry for the PS99 model. The upper layer is (stably) stratified, the lower layer is homogeneous and the interface is allowed to intersect the bottom topography. While the general equations include a β -plane term, our numerical study assumes a constant Coriolis parameter, f_0 .

parameter, which measures the destabilizing effect of baroclinicity relative to the stabilizing influence of topography. To leading order, the upper layer dynamic density, vertical velocity and horizontal velocity are given by, respectively,

$$(2.5) \quad \rho = -\phi_z, \quad w = -N^{-2}[\phi_{zt} + \mu J(\phi, \phi_z)], \quad \mathbf{u}_1 = \mathbf{e}_3 \times \nabla \phi,$$

while the lower layer velocity is given by

$$(2.6) \quad \mathbf{u}_2 = \mathbf{e}_3 \times \nabla [h_B + \mu(\phi|_{z=-1} + h)].$$

With the additional assumption of a homogeneous upper layer, a similar derivation results in the Swaters [38] two-layer baroclinic model, where the leading order balance on a β -plane is given by

$$(2.7) \quad \Delta \eta_t + \mu J(\eta, \Delta \eta + \beta y) + J(\eta + h, h_B) = 0,$$

$$(2.8) \quad h_t + J(\mu \eta + h_B, h) = 0.$$

Here, $\eta(x, y, t)$ is the upper layer geostrophic pressure, with other quantities and notation the same as before. As we show in the

Appendix, one can easily demonstrate that the equations (2.1) through (2.4) reduce to equations (2.7) and (2.8) in the limit of vanishing z -dependence in the upper layer. We also remark that a detailed and rigorous development of two-layer frontal geostrophic theory, which includes (2.7) and (2.8), from the primitive equations on a sphere, may be found in Karsten and Swaters [16]. For convenience, in the rest of the paper we will refer to equations (2.1) through (2.4) as the PS99, while (2.7) and (2.8) will henceforth be referred to as the S91 model.

In what follows we assume constant stratification in the upper layer, i.e., $N = \text{const.}$, and an x -invariant bottom topography, $h_B = h_B(y)$. While more realistic choices can be made for application to specific oceanographic settings, at present we wish to study the models with this simplified configuration. Since our main focus will be the SOG, which exhibits relatively small spatial scales, we will also make the f -plane approximation, i.e., $\beta = 0$. Given h_* , the scale height of the bottom layer and H , the scale height of the entire fluid column, we can define the depth ratio, $\delta = h_*/H$. The interaction parameter, μ , can then be expressed as $\mu = \delta/s$ (see Poulin and Swaters [24]), or equivalently, h_*/h_B^* , where s is a typical scaled bottom slope while h_B^* is the scale height of the bottom topography. In the numerical results of Sections 4 and 5, it is assumed that $\mu = 1.0$, following Karsten et al. [15].

For the purposes of numerical integration, the PS99 governing equations are reformulated as follows

$$(2.9) \quad q_t = \mu J(q, \varphi),$$

$$(2.10) \quad \rho_t = \mu J(\rho, \varphi), \quad z = 0,$$

$$(2.11) \quad \rho_t = \mu J(\rho, \varphi) - N^2 J(h_B, \varphi + h), \quad z = -1,$$

$$(2.12) \quad h_t = J(h, \mu\phi + h_B) + k_1 \Delta h + k_2 \Delta^2 h, \quad z = -1,$$

where $q = \Delta\varphi + N^{-2}\varphi_{zz}$ is the upper layer potential vorticity and $\rho = -\varphi_z$ is the upper layer dynamic density, (i.e., the density which is in hydrostatic balance with the leading order upper layer reduced pressure). The system is integrated forward in time using the Leapfrog scheme, with the Arakawa [1] formula for the Jacobian terms and

Robert smoothing (Asselin, [3]) at every time step to filter out the computational mode. Horizontal and biharmonic numerical friction (with typical coefficients of 10^{-6} and 10^{-8} , respectively) have been introduced into the evolution equation for h in order to damp out small scale noise. At each iteration, φ is recovered from q and ρ via a multigrid elliptic solver.

Our numerical experiments were performed in an x -periodic channel with no-normal flow boundary conditions on the walls. The length of the channel was chosen such that it allowed at least two wavelengths of the most unstable mode. There are two types of potential energy associated with the lower layer, defined nondimensionally as

$$(2.13) \quad PE_1(t) = \frac{1}{\mu} \iint h_B h \, dx dy$$

and

$$(2.14) \quad PE_2(t) = \frac{1}{2} \iint h^2 \, dx dy,$$

where the integration is over the horizontal extent of the domain. PE_1 is the energy released as the dense fluid descends down the sloping topography, and is the only source of energy for perturbation growth in this model. One may easily show that, without a source of lower layer fluid, PE_2 is an invariant of the system (see Poulin and Swaters [24]). Having specified a suitable profile for the lower layer height and no mean flow in the upper layer, ($\varphi \equiv 0$), the upper layer pressure was seeded with a superposition of waves with random amplitudes and phase shifts, in order to excite the instability. Initially the upper layer total energy,

$$(2.15) \quad E(t) = \iiint \nabla\varphi \cdot \nabla\varphi + N^{-2}(\varphi_z)^2 \, dx \, dy \, dz,$$

was equal to 10^{-12} times PE_2 as defined above. This ensured that the dominant wavelength for the flow emerged before nonlinear effects became significant. The horizontal resolution varied somewhat between simulations; however, a typical $28 \text{ km} \times 28 \text{ km}$ domain was discretized into a 120×120 grid, which yields a grid spacing of approximately 0.2 km. The vertical resolution was maintained at 16 levels (giving roughly 24 m per level).

A similar procedure was adopted for the S91 model, with obvious modifications appropriate for constant density in the upper layer. Numerical investigations of mesoscale gravity currents which employ the Swaters [38] model can be found in Karsten et al. [15], Swaters [39] as well as Choboter and Swaters [6]. Our discussion of such simulations is therefore brief.

3. Analysis of a Wedge Front. We consider an idealized flow where the lower layer thickness has the x -invariant form,

$$(3.1) \quad h_0(y) = 1 - \gamma y,$$

with linearly sloping bottom topography,

$$(3.2) \quad h_B(y) = \nu y,$$

for constants γ and ν in a periodic channel with $-L < y < L$. As was shown by Poulin and Swaters [24] for the linear stability problem associated with this wedge-like frontal profile and zero initial upper layer mean flow, the perturbation quantities, φ' and h' , have the exact normal mode solutions,

$$(3.3) \quad \varphi' = A \sin \frac{n\pi(y+L)}{2L} \cosh \lambda z \exp[ik(x-ct)] + c.c.,$$

$$(3.4) \quad h' = \frac{-A\gamma\mu}{c+\nu} \sin \frac{n\pi(y+L)}{2L} \cosh \lambda \exp[ik(x-ct)] + c.c.,$$

where A is an arbitrary constant,

$$(3.5) \quad \lambda^2 = N^2 \left(k^2 + \left(\frac{n\pi}{2L} \right)^2 \right),$$

and $c = c_R + ic_I$ is the complex phase speed. Here k is the along-channel wavenumber, $(n\pi/2L)$ is the quantized cross-channel wavenumber, ($n = 1, 2, 3, \dots$), and $c.c.$ refers to the complex conjugate. The corresponding dispersion relation is given by

$$(3.6) \quad c = \frac{-\nu(T + N^2) \pm \sqrt{\nu^2(T - N^2)^2 + 4\nu\gamma\mu N^2 T}}{2T},$$

where $T = \lambda \tanh \lambda > 0$.

While the assumed basic profile (3.1) does not actually intersect the bottom, it nevertheless demonstrates several important characteristics of the model. For instability to occur, ($c_I > 0$), the product of ν and γ must be negative so that the bottom topography must slope in the same sense as the interface. This is in contrast to instability of surface currents, where the front is often stabilized if the interface and topography gradients are positively correlated (e.g. Reszka and Swaters [28]). For a fixed δ and γ , we see that as $\mu = \delta/s$ decreases, so does the range of wavenumbers, k , for which the system is unstable. Indeed, we found that there exists a minimum μ , which is required for instability,

$$(3.7) \quad \mu_{\min} = \frac{-\nu(T - N^2)^2}{4\gamma N^2 T}.$$

For any γ, ν and λ with $\gamma\nu < 0$ as μ approaches $\mu_{\min} > 0$ from above, the front becomes unconditionally stable to perturbations. In this configuration, therefore, increasing the scale, s , of the bottom slope has a stabilizing effect. A stable region is of interest physically, since in real oceanographic settings, bottom-trapped flows are known to propagate significant distances before undergoing instability. With respect to the baroclinic processes we are describing then, the above analysis suggests that steep topography and/or a deep ambient layer can serve to maintain the stability of such a current.

The corresponding linear stability analysis for the S91 model was presented in Mooney and Swaters [23]. As $N \rightarrow 0$ in the above dispersion relation, we recover the Mooney and Swaters [23] result, which is to be expected given that the PS99 reduces to the S91 model in this limit. Typical growth rate curves for the two models are shown in Figure 2, with $N^2 = 0.2, 1.0$ and 2.0 for the continuously PS99. It is evident that the two main effects of allowing stratification, or increasing it, in the upper layer are to increase the along-channel wavenumber of the most unstable mode, as well as to increase the growth rate of that mode (Poulin and Swaters [24]). Because stratification inhibits vertical motions, increasing the stratification enhances the relative stretching/compression of fluid columns, thus leading to a more intense, localized instability (Lane-Serff and Baines [20]). Likewise, the low- and high-wavenumber cutoffs are increased, as is the range of along-shelf wavenumbers, k , which are unstable. We remark that, in the

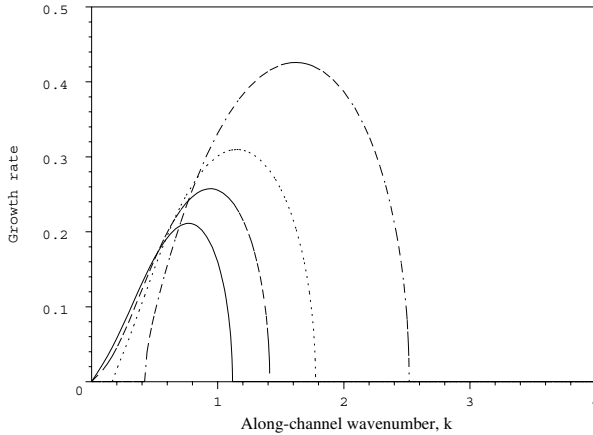


FIGURE 2. Analytical growth rates for instability on a wedge front, with $\mu = 1$, $\gamma = 0.1$, $\nu = -1.0$, $n = 1$ and $L = 2.0$. Solid line corresponds to the S91 model. Dash, dot and dash-dot lines are for the PS99, with $N^2 = 0.2$, 1.0 and 2.0, respectively.

continuously stratified case, the low cut-off for the total wavenumber, λ , is strictly positive, since n is always nonzero. However, the low-wavenumber cutoff for k does in fact vanish for N small enough.

By numerically integrating the PS99 governing equations (2.1)–(2.4) forward in time, we have verified that the structure of the perturbation which emerges from a random wavefield of negligible amplitude is in fact described by (3.3) and (3.4). The development of upper layer pressure at $z = -1$ is shown for nondimensional times 0, 10, 20 and 50 in Figure 3. Here the nondimensional channel width and length are 4.0 and 10.7, respectively, with $\mu = 1.0$, $\gamma = 0.1$, $\nu = -1.0$ and $N^2 = 1.0$. By $t = 50$, the normal mode solution (3.3) has emerged, with an along-channel wavenumber of approximately 1.2, which is the theoretical most-unstable wavenumber, as Figure 2 shows (dotted line). The dominant cross-channel structure is clearly the gravest, ($n = 1$), mode.

We determined the corresponding growth rate by computing, at each time step,

$$(3.8) \quad \sigma \simeq \frac{d}{dt} \ln \left(\sqrt{\frac{E(t)}{E(0)}} \right),$$

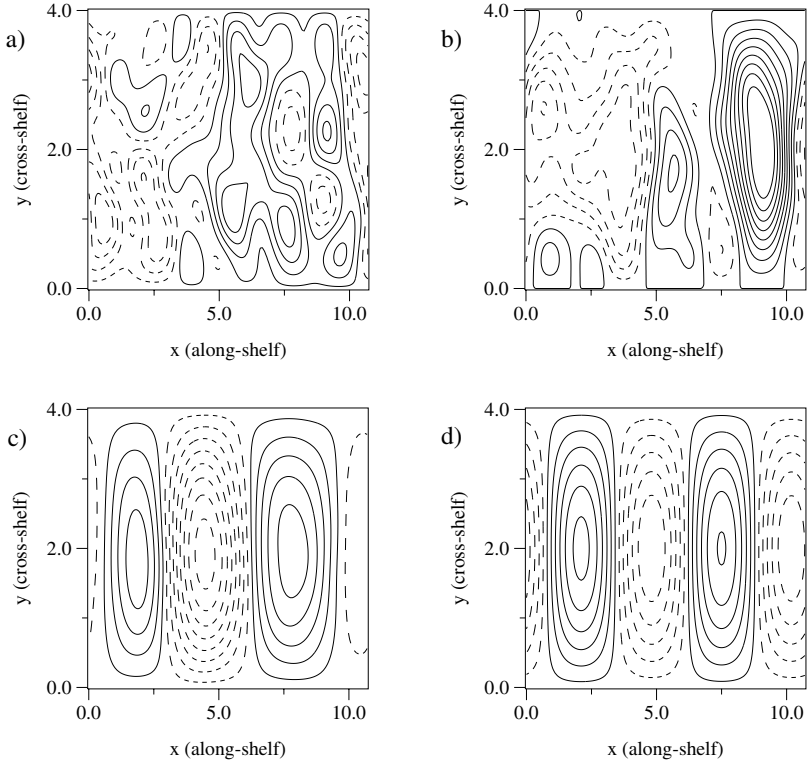


FIGURE 3. Contour plots of upper layer pressure, i.e., the growing perturbation, at $z = -1$ for a wedge-front, using the PS99 model, at nondimensional times (a) 0, (b) 10, (c) 20 and (d) 50. The contour range and interval are, respectively, (a) 3.0×10^{-10} , 4.0×10^{-11} , (b) 1.1×10^{-9} , 8.0×10^{-11} , (c) 1.0×10^{-8} , 8.0×10^{-10} and (d) 9.1×10^{-5} , 8.0×10^{-6} . Dashed contours correspond to negative values.

where the volume-averaged upper layer perturbation energy, $E(t)$, is given by (2.15). The growth rate, σ , is plotted versus time in Figure 4 (dashed line). It starts near zero, then increases and levels off at $t = 25$, with a final value of approximately 0.32. This is quite close to the analytical value of 0.31, resulting from the dispersion relation (3.6). Moreover, the high/low pressure cells seen in Figure 3 propagate in the positive x -direction at a nondimensional speed of 0.91, which compares favorably with the analytical value, 0.87.

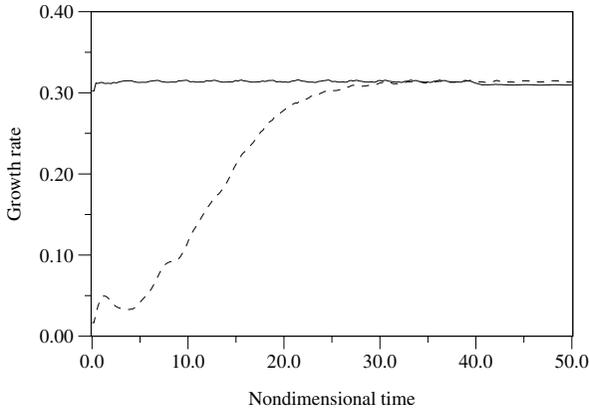


FIGURE 4. Perturbation energy versus nondimensional time, for two wedge-front simulations. Dashed line (a) corresponds to the simulation in Figure 3. Solid line (b) corresponds to the simulation where the analytical perturbation solution was used as the initial condition.

If we start the simulation using the exact solution (3.3) and (3.4) with the most unstable wavenumber, $k = 1.2$, then the growth rate during the linear stage of growth is almost exactly 0.31, as predicted by the dispersion relation (3.6). The growth rate for this simulation is also included in Figure 4 for comparison (solid line). It is worth noting that the upper layer perturbation preferentially amplifies at the bottom of the layer, thus giving the developing high/low pressure cells a somewhat conical appearance. A vertical cross-section at $y = 2.0$, $t = 50.0$ of the upper layer streamfunction is plotted in Figure 5. This tapered vertical structure is also ubiquitous in the SOG simulations, described in the following section.

4. Strait of Georgia results. The SOG is a long, narrow body of water, with dimensions of roughly 40 km by 280 km. The SOG connects with the ocean primarily through Juan de Fuca Strait in the south (see Figure 6) and is largely restricted by islands at its northern end. Typical depths for the central part of the strait are 300–400 m, and shallow sills prevent free exchange with continental shelf waters. Estuarine circulation is primarily driven by freshwater discharge from the Fraser River. Tidal currents, formation of fronts, and deep water renewal are all known to occur in the SOG, (LeBlond et al. [37], and

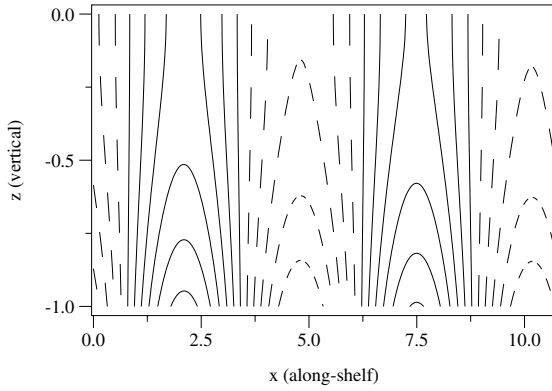


FIGURE 5. Vertical cross-section of upper layer pressure corresponding to Figure 3(d). Bottom-intensified structure of the upper layer pressure cells is clearly visible. Dashed lines correspond to negative values.

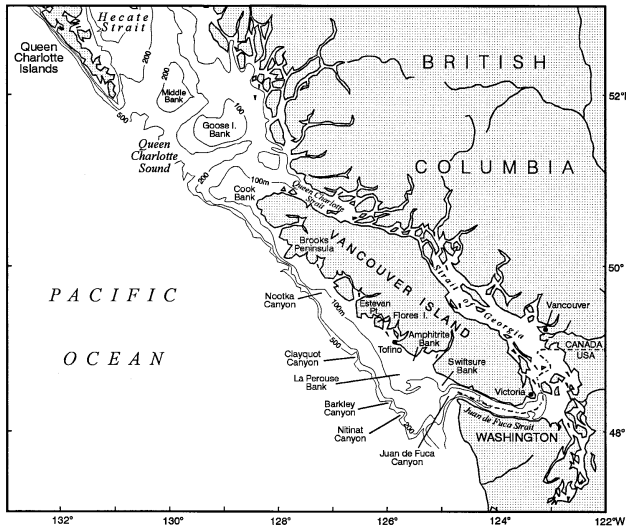


FIGURE 6. Coastal geography of southern British Columbia, Canada. The Strait of Georgia is located between Vancouver Island and the mainland. Reproduced from Figure 1 in Foreman and Thomson [8].

references therein). Of particular interest here is the low-frequency variability of the deep currents, as reported by Stacey et al. [35].

To investigate the role of baroclinic instability in the observed fluctuations, Karsten et al. [15] performed a linear instability calculation, employing the S91 model in a configuration appropriate for the central SOG. The cross-channel shape of the bathymetry was approximated by a piecewise-linear trough (with its minimum in the interior of the channel), as shown in Figure 7a. The deep current was assumed to have a parabolic profile and was initially situated entirely on one (linear) slope of the topography. Data from Stacey et al. [35] clearly indicate that the most intense pulses of deep water intruding into the SOG basin were detected on its eastern side, consistent with the supposition that the bottom-trapped flow travels along sloping topography with the shallow water on its right. As part of their analysis, Karsten et al. [15] found that the instability takes the form of wavelike undulations of the incroppings, which are greater on the down-slope side than the up-slope side. The most unstable mode was found to be about $k = 1.1$, which corresponds to a dimensional wavelength of about 40 km. It was thought that these undulations may grow into eddies, whose diameter would be 20 km (half of 40 km), or about twice as large as the observational record indicates.

Because eddy formation is intrinsically a nonlinear process, we integrated the S91 equations (2.7) and (2.8) on an f -plane numerically, using the same basic state and parameter values as those suggested in Karsten et al. [15]. The lower layer was initialized as

$$(4.1) \quad h_0(y) = \max(1.0 - (y - 2.25)^2, 0),$$

which corresponds to a 14 km wide, x -invariant gravity current with a maximum thickness of 65 m and its axis at $y = 15.75$ km. Given this profile, the average initial velocity is 18 cm/s, typical of deep flows in the region. The nondimensional form of the topography was piecewise linear,

$$(4.2) \quad h_B(y) = \begin{cases} 2(1 - y) & 0 < y < 1, \\ y - 1 & 1 < y < 4, \end{cases}$$

which has a dimensional maximum of 189 m at $y = 28$ km and vanishes at $y = 7$ km. The instability initially progressed according

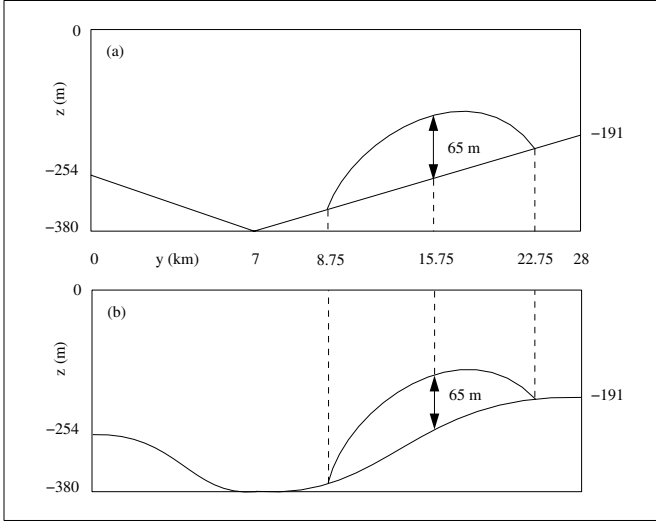


FIGURE 7. Cross-shelf sections of the (a) piecewise-linear trough and (b) smooth topography used in our SOG simulations.

to the Karsten et al. [15] linear theory, producing undulations of the incroppings, especially on the down-slope side. We found, however, that lower layer fluid which reached the discontinuity in the topographic gradient at $y = 7$ km was immediately sheared away. This is not surprising, given that the lower layer velocity, (2.6) (with $\phi|_{z=-1}$ replaced by η), is heavily influenced by the bottom slope when η and h are small. The abrupt change in bathymetry effectively acts as a barrier and inhibits the gradual evolution of the growing plumes. Since this topography is rather unrealistic, it will not be considered further.

The S91 model was then integrated numerically using the following smooth topography (in nondimensional units)

$$(4.3) \quad h_B(y) = \begin{cases} (1.0 + \cos(\pi y)) & 0 < y < 1, \\ 3(1.0 + \cos[(1/3)\pi(y - 4)])/2 & 1 < y < 4. \end{cases}$$

This function approximates the SOG bathymetry in the region of interest and corresponds to the same fluid depths at $y = 0, 7$ and 28 km as (4.2). Unlike the piecewise-linear topography, (4.3) is continuously differentiable (see Figure 7b). The channel dimensions were 4.0×11.4

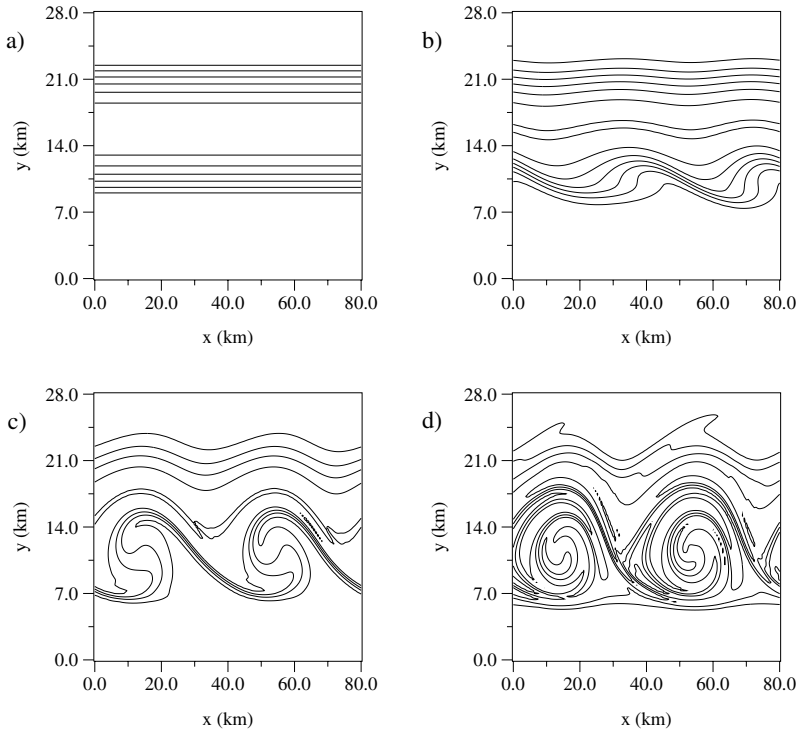


FIGURE 8. Contour plots of h for the S91 SOG simulation using the smooth topography at (a) 0, (b) 17.5, (c) 19.3 and (d) 23.0 days. The contour range is 0 to 65 m. The contour interval is 10 m in (a) and (b) and 15 m in (c) and (d).

for a dimensional width and length of 28 km and 80 km, respectively. Figure 8 depicts four contour plots of the lower layer thickness for this simulation for days 0, 17.5, 19.3 and 23.0. In Figure 8a, we see the undisturbed coupled front, which at this stage rests entirely on one slope of the trough. The down-slope incropping has deformed in Figure 8b yielding two waves of the most unstable mode. The wavelike perturbation moves with the current, i.e., in the negative x -direction, at a speed of roughly 12 cm/s, in agreement with Karsten et al. [15]. As these protrusions grow, they subsequently encounter the opposite face of the valley and begin to roll up on themselves in a spiral-like pattern, (Figure 8c). This process continues and the flow eventually reaches a quasi-steady state in Figure 8d. For the initial phase of growth, we

estimate e-folding times of approximately 15 h. In the end, the spiral structures have a wavelength of 40 km, though individual filaments exhibit much smaller lengthscales.

In Figures 9a–d we plot the upper layer pressure corresponding to the same times as Figure 8a–d. Figure 9a shows the initial random perturbation with small amplitude, (about 10^{-6}). The upper layer streamfunction quickly organizes itself into 2 pairs of high/low pressure cells, (Figure 9b), which intensify as the gravity current gives up its available gravitational energy, (Figures 9c and d). These pressure cells clearly indicate strong cyclonic and anticyclonic circulations in the upper layer; however, their wavelength is about 20 km, as predicted by Karsten et al. [15]. A number of factors may account for the discrepancy between this result and the Stacey et al. [36] analysis, such as the simplifying assumption of x -invariant topography. However, the oblong “eddies” in Figures 9c and d extend over the entire width of the channel and are therefore qualitatively different from the localized vortices described in Stacey et al. [36]. As was pointed out in Section 3, the lengthscales associated with the PS99 tend to be smaller than in the S91 model, at least in the case of a uniform bottom flow. The nonlinear evolution of a coupled front in the in the continuously-stratified context is therefore of interest.

In a series of simulations we employed the PS99 with the same configuration (4.1) and (4.3) in order to determine the effects of ambient stratification on the instability process. The Burger number, N^2 , was set to 0.65 which yields stratification roughly in agreement with vertical σ_t sections in the northern part of the SOG, (LeBlond et al. [37]). The width of the channel was 28 km as in the S91 simulation. The channel length was reduced to 28 km which allowed 3 wavelengths of the most unstable mode. Contour plots of the lower layer thickness for 8.7, 10.6, 12.4 and 14.3 days are depicted in Figure 10. The initial lower layer profile was the same as in the S91 case and is thus not shown. The dominant along-channel wavenumber which emerges is 3.1, about three times the value obtained for the S91 model. This gives a dimensional wavelength of approximately 9 km (Figure 10a). Again, the down-slope deformations can be seen to grow and break backwards in relation to the direction of flow. Between 8.7 and 10.6 days the instability is temporarily saturated and the wavelike perturbations merge, increasing the dominant wavelength (Figure 10b). This behavior is a result of

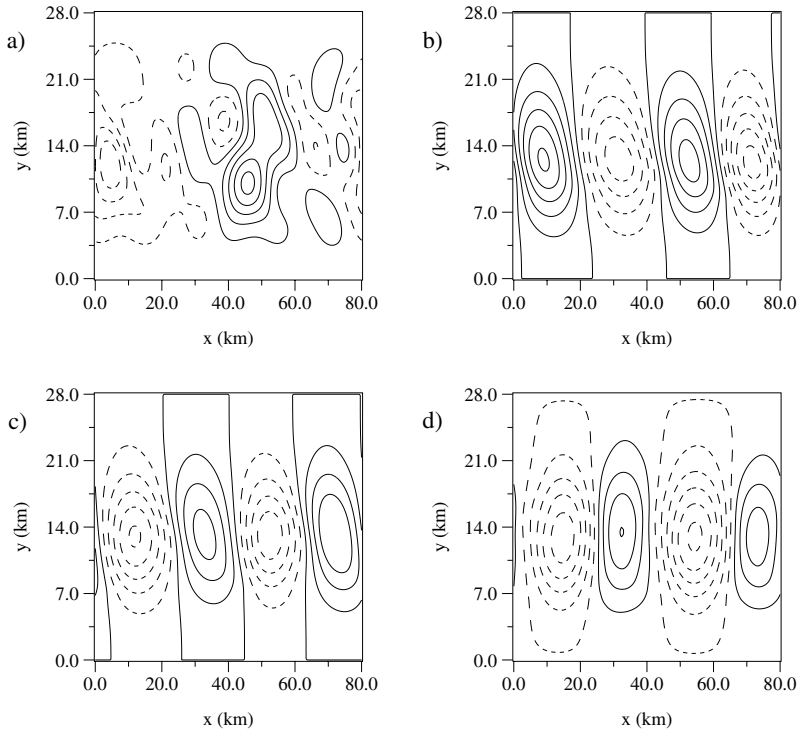


FIGURE 9. Contour plots of p for the simulation corresponding to Figure 8. The contour range and interval are, respectively, (a) 2.0×10^{-6} , 2.0×10^{-7} ; (b) 0.2, 0.02, (c) 0.7, 0.08 and (d) 0.9, 0.1. Dashed contours correspond to negative values.

the up-scale energy cascade (Rhines [29]) and will be discussed more fully in the following sections. We point out that a general theory for weakly-nonlinear saturation of instabilities in frontal geostrophic models is presented in Karsten and Swaters [17] and [18]. As cyclonic vorticity is concentrated behind the wave crests, the roll-up process continues in Figure 10c and eventually destroys the mean flow, giving rise to a single irregular gyre (Figure 10d).

The evolution of the upper layer pressure at $z = -1$, (dimensionally, $z = -H$), is given in Figure 11. The initial random wave field first develops into a train of alternating high and low pressure cells, (Figure 11a) at $y \approx 10$ km. These propagate in the negative x -

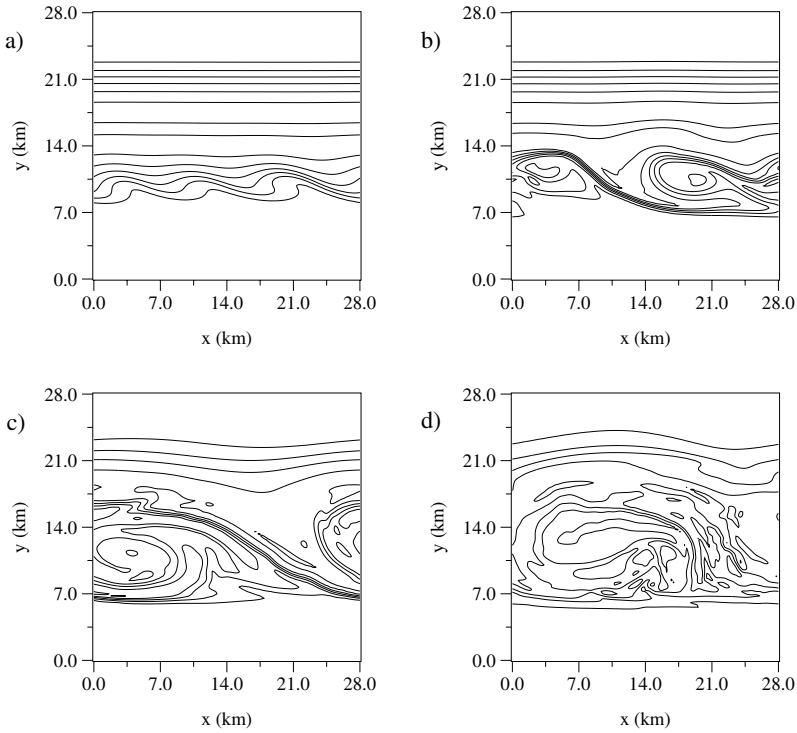


FIGURE 10. Contour plots of h for the SOG simulation using the continuously PS99 with smooth topography, at (a) 8.7, (b) 10.6, (c) 12.4 and (d) 14.3 days. Contour range is 65 m. Contour intervals are 8.5 m in (a) and (b) and 12 m in (c) and (d).

direction at around 7 cm/s. We have found that this stage of the instability is very rapid, with e-folding times of 7 hours, about half that predicted by the S91 model. The vortices are highly localized, unlike the ones in Figures 9c–d. The formation of small eddies at the onset of the instability is in good agreement with the Stacey et al. [36] analysis. E-folding times of less than a day also compare favorably with fluctuations of the deep currents in the SOG. The eddies merge in Figure 11b and again in Figure 11c while they continue to intensify. The resulting eddy dipole persists for the next several days without significant change (Figure 11d). Growth at the larger lengthscales was found to be an order of magnitude slower than the initial instability.

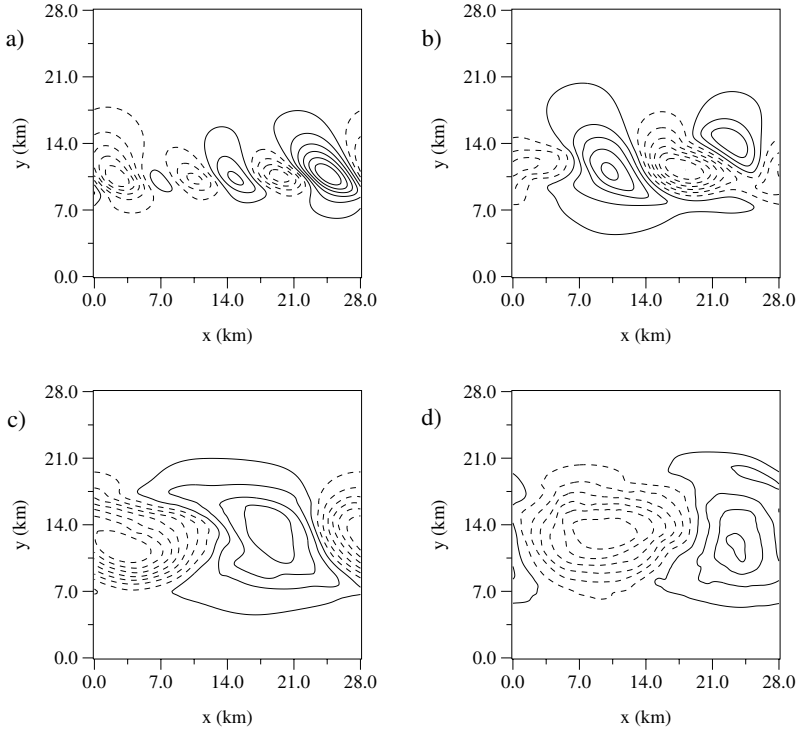


FIGURE 11. Contour plots of upper layer pressure at the bottom of the fluid column for times corresponding to Figure 9. The contour range and interval are, respectively, (a) 0.12, 0.01, (b) 0.44, 0.04, (c) 0.92, 0.08 and (d) 1.01, 0.1. Dashed contours correspond to negative values.

Analysis of the current meter data (Stacey et al. [35]) does indicate a basin-wide gyre at middepth, as well as a clockwise/counterclockwise oscillation of the mean velocity field, which may be related to the slowly-propagating, domain-scale dipole evident at late times in our simulations. We hasten to add however that, in reality, wind stress and tides (as well as their nonlinear interactions) constantly inject energy into high frequency/wavenumber motions. Because our model neglects such external forcing, we are inclined to focus mainly on the initial and intermediate stages of the simulations.

Based on their observational data, Stacey et al. [37] estimated the e-folding times of barotropic and baroclinic transfers to be about 1 – 4

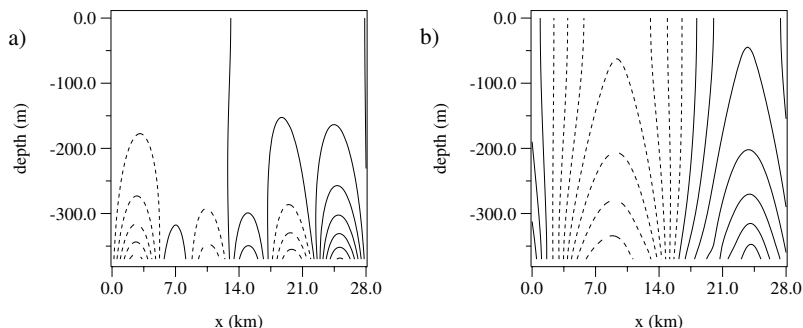


FIGURE 12. Vertical cross-sections of upper layer pressure corresponding to Figure 10. Plot (a) corresponds to Figure 10 (a) while plot (b) corresponds to Figure 10(d).

days. However, it must be stressed that their baroclinic growth rate calculation was based entirely on density and velocity correlations. The baroclinic process we are modeling here, and which we believe is operative in the SOG, is the release of gravitational potential energy by a dense fluid mass that descends down a topographic slope. The growth rates associated with this mechanism may indeed be higher than the Stacey et al. [37] estimate suggests. Given that the deep current fluctuations in the SOG exhibit a highly nonlinear, almost turbulent character (Stacey et al. [35]), we believe that e-folding times of less than a day are not unreasonable.

The emergent vortices in the stratified layer are clearly bottom-intensified. For example, the maximum dimensional velocity in Figure 11d is 36 cm/s and occurs at the bottom of the upper layer, while the velocities for the same time frame at the top of the fluid column are only half as large. Vertical cross-sections of the upper layer pressure corresponding 8.7 and 14.3 days are given in Figures 12a and b. The observed tapered structure highly resembles analytical eddy solutions for the PS99 model found by Poulin and Swaters [25]. Indeed, numerous bottom-intensified vortices were reported by Stacey et al. [36]. The ability to describe this vertical structure is another strength of the PS99 model.

5. Instability mechanism. In order to better understand the instability process operative in the PS99 model, we performed a number

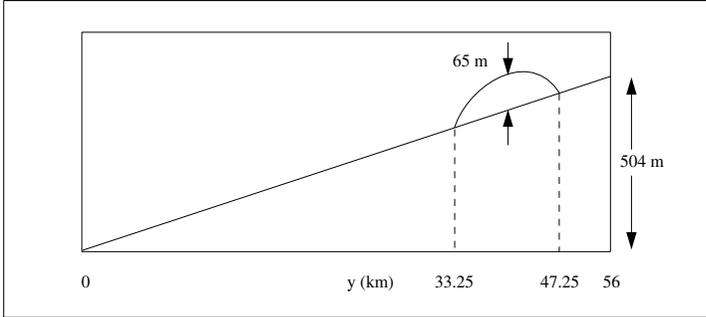


FIGURE 13. Cross-channel section of the linearly-sloping topography.

of simulations with a linearly sloping bottom, nondimensionally given by

$$(5.1) \quad h_B = y,$$

for an unscaled slope of 9 m/km. A diagram of the geometry appears in Figure 13. While this bottom topography is not applicable to the Strait of Georgia itself, we utilize the same scalings as in previous simulations for comparison purposes. The domain was 56 km \times 28 km, i.e., wide enough so that boundaries did not impede the downward slumping of dense fluid and long enough to allow two wavelengths of the initial instability. We note that the simulation was also performed in a longer channel (not shown) with similar results.

The evolution of the lower layer thickness, h , for this simulation is given in Figures 14a–d, corresponding to days 0, 7.4, 10.1 and 12.2, respectively. The undisturbed gravity current appears in Figure 14a. Deformation of the downslope incropping is evident in Figure 14b, corresponding to a wavelength of 14 km. This lengthscale is larger than the dominant wavelength obtained for the SOG simulations (see previous section). Our tests indicate that instability characteristics for the PS99 model are heavily influenced by the topographic gradient directly beneath the downslope incropping. The cross-channel slope of the SOG topography (4.3) at the downslope incropping (nondimensionally, $y = 1.25$) has a value of 0.41. On the other hand, the slope of the linear topography (5.1) is everywhere 1.0. The fact that the

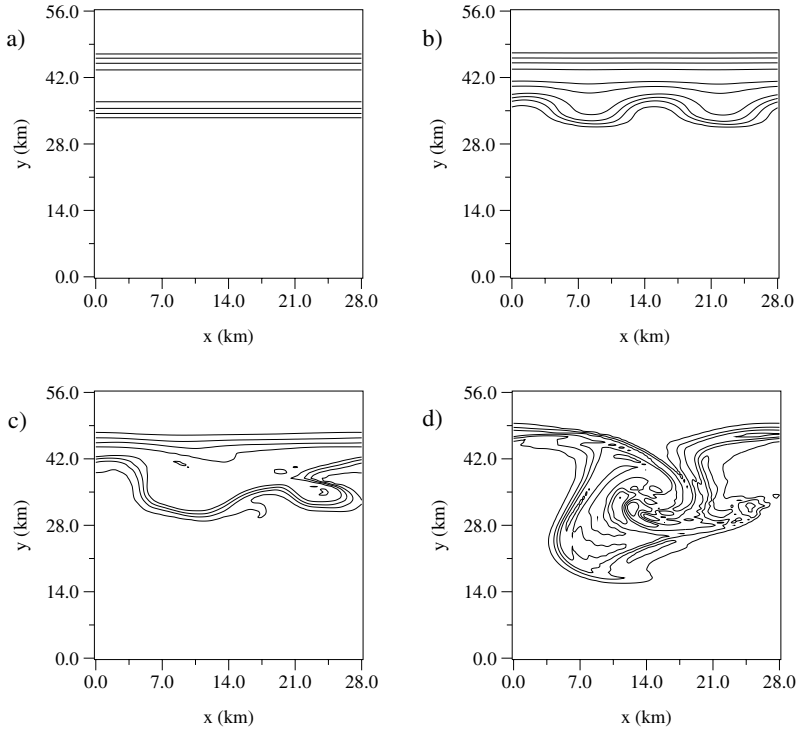


FIGURE 14. Contour plots of lower layer thickness for the simulation using the continuously PS99, with linearly-sloping topography. The frames correspond to (a) 0, (b) 7.4, (c) 10.1 and (d) 12.2 days. The contour range is 65 m. The contour interval is 15 m in all four plots.

most unstable wavenumber is lower in the present simulation is therefore consistent with the observations made in Section 3 regarding the interaction parameter, μ . An important aspect of the instability we are modeling is that no topographic variation is needed to destabilize the flow. With regard to the SOG however, it is likely that an irregular bathymetry introduces more spatial variability than that which is demonstrated in our numerical study.

As in the SOG simulations, the initial instability saturates and a shift to larger scales occurs between days 7.4 and 10.1, so that the perturbed incropping is dominated by a single deformation in Figure 14c. Further growth occurs at the larger lengthscale, leading to destruction of

the mean flow and the development of a single spiral-like feature, rotating anticyclonically, Figure 14d. This is not unlike results obtained numerically for the S91 model in Swaters [39]. Though not shown, the upper layer streamfunction evolves similarly to the SOG simulations, as in Figure 11. A train of eddy anomalies develops in the region of the downslope incropping and intensifies throughout the simulation. The four upper layer eddies which exist at 7.4 days merge into two by 10.1 days, not unlike the merger indicated by Figures 11b and c. The nonlinear cascade, which leads to larger lengthscales in rotating systems, was discussed at length in the quasigeostrophic context by Rhines [29] and has been noted in other numerical studies of unstable oceanic currents by Ikeda et al. [13], Samelson and Chapman [30] and others.

The growth of perturbations in the PS99 model (as in the S91 model) relies on the release of gravitational potential energy associated with the dense fluid descending down the slope. The time evolution of the lower layer gravitational potential energy (2.13) is plotted in Figure 15a while in Figure 15b we plot the time evolution of the perturbation energy, that is, the upper layer total energy (2.15). Both energies have been normalized by the total system energy (see below). The perturbation energy clearly grows by many orders of magnitude. The two peaks visible in Figure 15b correspond to the two successive episodes of instability at approximately 8 and 12 days, as described above. Comparison of Figure 15a and b shows the close correlation between increases in $E(t)$ and the decreases in $PE_1(t)$. This is to be expected, given that $PE_1(t)$ is the only source of energy available for the growth of perturbations. Indeed, in Figure 15c we plot the computed total system energy, defined as $PE_1 + PE_2 + E$ versus time, normalized by its initial value. While a small amount of fluctuation, due to numerical effects, is evident at late times in the simulation, the system energy is conserved with reasonable accuracy during the entire instability process. Figure 15d shows the time evolution of the nondimensional y -coordinate of the lower layer center of mass, whose initial value is $y = 5.75$, i.e. the same as the center of the current profile at the start of the simulation. As the instability progresses, the y -moment of the dense fluid decreases, indicating a gradual descent of the evolving gravity current into deeper water. Again, we see the two local maxima that correspond to temporary saturation of the instability. The

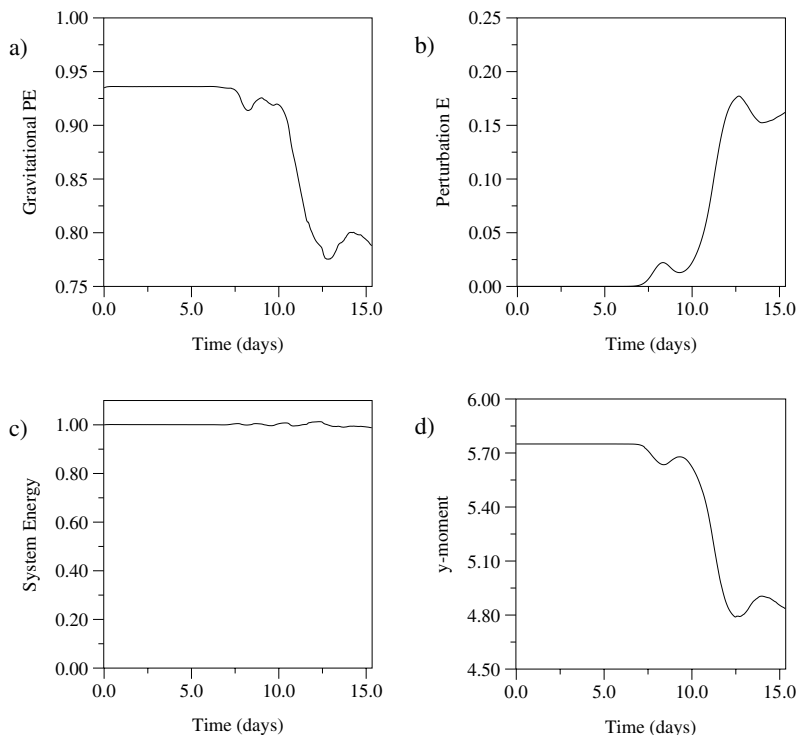


FIGURE 15. Diagnostics for the simulation with linearly sloped topography: (a) normalized gravitational potential energy of the lower layer, (b) normalized perturbation energy (i.e. total energy of the upper layer), (c) normalized total system energy, (d) nondimensional y -moment of the lower layer. All quantities are defined in the text.

location of these extrema and the overall shape of the curve are in good agreement with Figure 15b (as well as 15a), further emphasizing the direct link between the cross-shelf migration of the dense fluid and the growth of perturbations.

6. Conclusions. We have shown that the baroclinic theory of Swaters [38] is a limiting case of the continuously-stratified model of Poulin and Swaters [24]. The latter reduces to the former as stratification vanishes in the ambient fluid. Results of simulations employing both models, pertaining to fluctuations of deep currents in

the Strait of Georgia are generally in agreement with the analysis of Stacey et al. [35], [36]. We have found that the baroclinic mechanism described here leads to the development of eddies of both signs, with diameters of a few kilometers. However the dominant lengthscales in the continuously stratified model with moderate values of the Burger number are a factor of 2 – 3 smaller than those intrinsic to the earlier Swaters [38] theory. The shorter along-channel lengthscales are more in keeping with the Stacey et al. [36] study, indicating that the continuously stratified theory is better suited to the description of variability in the SOG. Moreover, in the continuously stratified context, the eddies which emerge in the upper layer are highly localized in space and exhibit a tapered vertical structure. Both of these characteristics are consistent with the Stacey et al. [35] observations.

The first phase of instability is very rapid (e-folding times of less than 10 hours) which increases the likelihood that vortices can form before external forces, such as tides, alter the flowfield. After weakly nonlinear interactions induce a shift to larger scales, further instability destroys the mean flow and leads to an irregular but coherent patch of fluid, rotating anticyclonically. However, we found that in a narrow channel such as the SOG, the topography tends to decrease growth rates in the second stage of instability. This is because the reversal in slope effectively arrests the downward propagation of dense plumes and therefore the release of gravitational potential energy. Stacey et al. [37] also suggested that baroclinic processes may be inhibited by the relatively small size of the strait.

Localized, bottom-intensified eddies were also obtained in simulations that employed linearly-sloping topography, which roughly approximates a sloped continental shelf. The influence of the cross-shelf topographic gradient on the dominant along-channel wavenumber was consistent with a linear theory for a simple uniform current, for which analytical solutions were readily available. The linear analysis predicts that increasing the bottom slope stabilizes the flow, while decreasing the bottom slope increases the range of unstable wavenumbers. Numerical simulations also elucidated the relationship between the growth of perturbations and the gradual slumping of the dense fluid down the slope. It was found that the growth of perturbation energy is closely correlated with the cross-shelf center of mass associated with the lower layer. The potential energy released by the gravity current is converted

to potential and kinetic energy of the ambient ocean. Notably, we find that the instability mechanism presented here does not require any variations in the topography.

None of our simulations results in a turbulent eddy field, which the analysis of Stacey et al. [36] seems to imply. It is plausible that along-channel topographic variations, which we have neglected in this study, could introduce eddy motions which are more turbulent in character. The assumption of along-channel periodicity may also be too restrictive, since Deep Water replacement in the SOG tends to be episodic rather than continuous. Future work should include inflow/outflow conditions which are more reflective of actual mass exchanges with the ocean. The effect of variable coastlines and a z -dependent stratification frequency could also be investigated. More generally, it would be interesting to apply the model to the Denmark Strait Overflow, where significant amounts of cold, salty water cross into the Atlantic basin to become part of the North Atlantic Deep Water. Here, instabilities of the deep flow are frequent and often lead to eddy features with spiral surface signatures (Bruce [5]). It has been suggested (Spall and Price [33]) that strong cyclonic motion may be produced by vertical stretching of the water column downstream of the strait. Since the present model assumes that the upper layer is driven by vortex tube stretching associated with descending plumes of lower layer fluid (see Poulin and Swaters [24]), it may thus appropriately describe this aspect of Denmark Strait Overflow dynamics.

It is evident in simulations employing both the S91 and PS99 models that, given enough time, emergent eddies coalesce into larger ones, and that this trend continues up to the scale allowed by the domain. As mentioned previously, this is a result of the inverse energy cascade, typical of quasi-two-dimensional fluids. Momentarily setting aside issues such as a finite domain and external forcing, one may reasonably ask if there exists an upper bound on the growing lengthscale, as is true for flows on the β -plane in the frontal geostrophic limit (Cushman-Roisin and Tang [7], Tang and Cushman-Roisin [40]). As Karsten and Swaters [17] and [18] demonstrated, the appropriate analogue of the Rhines scale in S91, i.e., baroclinic, frontal geostrophic dynamics is

$$(6.1) \quad L_K = (\delta R_I^4 L_\beta^2)^{1/6},$$

where R_I is the internal Rossby radius, $L_\beta = f_0/\beta_0$ is the planetary scale and δ is the depth ratio, as before. The scale L_K separates

the possible models into two regimes with very different stability characteristics (Karsten and Swaters [17]). It would be of interest to determine whether, in the context of bottom-trapped flows, the limiting lengthscale is related to (6.1), with L_β replaced by an appropriate topographic scaling. We leave these questions for future investigations.

APPENDIX

To show that the PS99 model on a β -plane reduces to the S91 model on a β -plane in the limit of vanishing z -dependence, we first integrate (2.1) in z ,

$$(7.1) \quad \int_{-1}^0 [(\Delta\varphi + (N^{-2}\varphi_z)_z)_t + \mu J(\varphi, \Delta\varphi + (N^{-2}\varphi_z)_z + \beta y)] dz = 0.$$

Simplifying, we obtain

$$(7.2) \quad \begin{aligned} & \frac{\partial}{\partial t} \Delta \int_{-1}^0 \varphi dz + N^{-2} \varphi_{zt} \Big|_{z=-1}^{z=0} + \mu \int_{-1}^0 J(\varphi, \Delta\varphi) dz \\ & + \mu N^{-2} J(\varphi, \varphi_z) \Big|_{z=-1}^{z=0} - \mu \int_{-1}^0 N^{-2} J(\varphi_z, \varphi_z) + \mu\beta \int_{-1}^0 \varphi_x dz = 0, \end{aligned}$$

where the fourth and fifth terms are a result of integration by parts. Rearranging, and realizing that $J(A, A) \equiv 0$ for any differentiable function A ,

$$(7.3) \quad \begin{aligned} & \frac{\partial}{\partial t} \Delta \int_{-1}^0 \varphi dz + N^{-2} [\varphi_{zt} + \mu J(\varphi, \varphi_z)]_{z=0} \\ & - N^{-2} [\varphi_{zt} + \mu J(\varphi, \varphi_z)]_{z=-1} + \mu \int_{-1}^0 J(\varphi, \Delta\varphi) dz + \mu\beta \int_{-1}^0 \varphi_x dz = 0. \end{aligned}$$

Substituting the vertical boundary conditions (2.2) and (2.3) in the second and third terms respectively, the result is

$$\frac{\partial}{\partial t} \Delta \int_{-1}^0 \varphi dz + J(\varphi|_{z=-1} + h, h_B) + \mu \int_{-1}^0 J(\varphi, \Delta\varphi) dz + \mu\beta \int_{-1}^0 \varphi_x dz = 0.$$

Taking the limit as $\frac{\partial\varphi}{\partial z} \rightarrow 0$,

$$\Delta\varphi_t + \mu J(\varphi, \Delta\varphi + \beta y) + J(\varphi + h, h_B) = 0,$$

which is identical to the upper layer equation (2.7) for the two layer model (Swaters [38]) with the vertically-averaged φ playing the role of η . The lower layer equation (2.4) then becomes the same as the lower layer equation (2.8).

Acknowledgments. The authors wish to thank Paul Choboter for his valuable comments. Preparation of this manuscript was supported in part by a PGS A grant awarded to the first author by the Natural Sciences and Engineering Research Council of Canada, a Graduate Fellowship awarded to the first author by the University of Alberta, as well as a research grant awarded to the second author by the Natural Sciences and Engineering Research Council of Canada.

REFERENCES

1. A. Arakawa, *Computational design for long term numerical integration of the equations of fluid motion: Two-dimensional incompressible flow*, J. Comput. Phys. **1** (1966), 119–143.
2. L. Armi and E. D’Asaro, *Flow structures of the benthic ocean*, J. Geophys. Res. **85** (1980), 469–484.
3. R.A. Asselin, *Frequency filter for time integrations*, Mon. Weather Rev. **100** (1972), 487–490.
4. R.E. Britter and P.F. Linden, *The motion of the front of a gravity current travelling down at an incline*, J. Fluid Mech. **99** (1980), 531–543.
5. J.G. Bruce, *Eddies southwest of the Denmark Strait*, Deep-Sea Res. **42** (1995), 13–29.
6. P.F. Choboter and G.E. Swaters, *On the baroclinic instability of axisymmetric rotating gravity currents with bottom slope*, J. Fluid Mech. **408** (2000), 149–177.
7. B. Cushman-Roisin and B. Tang, *Geostrophic regimes and geostrophic turbulence beyond the radius of deformation*, in *Mesoscale/synoptic structures in geophysical turbulence* (J.C.J. Nihoul and B.M. Jamart, eds.), Elsevier, 1989.
8. M.G.G. Foreman and R.E. Thomson, *Three-dimensional simulations of tides and buoyancy currents along the west coast of Vancouver Island*, J. Phys. Oceanogr. **27** (1997), 1300–1325.
9. G. Gawarkiewicz and D.C. Chapman, *A numerical study of dense water formation and transport on a shallow, sloping continental shelf*, J. Geophys. Res. **100** (1995), 4489–4507.
10. R.W. Griffiths, P.D. Killworth and M.E. Stern, *Ageostrophic instability of ocean currents*, J. Fluid Mech. **117** (1982), 343–377.

11. T.W.N. Haine, A.J. Watson, M.I. Liddicoat and R.R. Dickson, *The flow of Antarctic bottom water to the southwest Indian Ocean estimated using CFCs*, J. Geophys. Res. **103** (1998), 27,637–27,653.
12. R.W. Houghton, R. Schlitz, R.C. Beardsley, B. Butman and J.L. Chamberlin, *The Middle Atlantic Bight cold pool: Evolution of the temperature structure during summer 1979*, J. Phys. Oceanogr. **12** (1982), 1019–1029.
13. M. Ikeda, W.J. Emery and L.A. Mysak, *Seasonal variability in meanders of the California current system off Vancouver Island*, J. Geophys. Res. **89** (1984), 3487–3505.
14. L. Jiang and R.W. Garwood, Jr., *Three-dimensional simulations of overflows on continental slopes*, J. Phys. Oceanogr. **26** (1996), 1214–1233.
15. R.H. Karsten and G.E. Swaters, *A unified asymptotic derivation of $S91$, frontal geostrophic models including planetary sphericity and variable topography*, Phys. Fluids **11** (1999), 2583–2597.
16. ———, *Nonlinear effects in $S91$, large-amplitude, geostrophic dynamics: Part 1. The strong-beta case*, J. Fluid Mech. **412** (2000a), 125–160.
17. ———, *Nonlinear effects in $S91$, large-amplitude, geostrophic dynamics: Part 2. The weak-beta case*, J. Fluid Mech. **412** (2000b), 161–196.
18. R.H. Karsten, G.E. Swaters and R.E. Thomson, *Stability characteristics of deep-water replacement in the Strait of Georgia*, J. Phys. Oceanogr. **25** (1995), 2391–2403.
19. P.D. Killworth, *Mixing on the Weddell Sea continental slope*, Deep Sea Res. **24** (1977), 427–488.
20. G. F. Lane-Serff, and P. G. Baines, *Eddy Formation by Overflows in Stratified Water*, J. Phys. Oceanogr. **30**, 2000, 327–337.
21. P.H. LeBlond, H. Ma, F. Doherty and S. Pond, *Deep and intermediate water replacement in the Strait of Georgia*, Atmos.-Ocean **29** (1991), 288–312.
22. S.G. Marinone and S. Pond, *A three-dimensional model of deep water renewal and its influence on residual currents in the Central Strait of Georgia, Canada*, Estuarine, Coastal and Shelf Science **43** (1996), 183–204.
23. C.J. Mooney and G.E. Swaters, *Finite-amplitude baroclinic instability of a mesoscale gravity current in a channel*, Geophys. Astrophys. Fluid Dynamics **82** (1996), 173–205.
24. F.J. Poulin and G.E. Swaters, *Sub-inertial dynamics of density-driven flows in a continuously stratified fluid on a sloping bottom, I. Model derivation and stability characteristics*, Proc. Roy. Soc. London **A455** (1999a), 2281–2304.
25. ———, *Sub-inertial dynamics of density-driven flows in a continuously stratified fluid on a sloping bottom, II. Isolated eddies and radiating cold domes*, Proc. R. Soc. Lond. **A455** (1999b), 2305–2329.
26. J.F. Price and M. O’Neil Baringer, *Outflows and deep water production by marginal seas*, Prog. Oceanog. **33** (1994), 161–200.
27. S. Rahmstorf, *Decadal variability of the thermohaline ocean circulation, in Beyond El Niño: Decadal and interdecadal climate variability* (A. Navarra, ed.), Springer, 1999.

28. M.K. Reszka and G.E. Swaters, *Eddy formation and interaction in a frontal geostrophic model*, J. Phys. Oceanogr. **29** (1999), 3025–3042.
29. P.B. Rhines, *The dynamics of unsteady currents*, in *The sea*, Vol. 6 (E.D. Goldberg, I.N. McCave, J.J. O'Brien and J.H. Steele, eds.), John Wiley, New York, 1977.
30. R.M. Samelson and D.C. Chapman, *Evolution of the instability of a mixed-layer front*, J. Geophys. Res. **100** (1995), 6743–6759.
31. G.I. Shapiro and A.E. Hill, *Dynamics of dense water cascades at the shelf edge*, J. Phys. Oceanogr. **27** (1997), 2381–2394.
32. P.C. Smith, *A streamtube model for bottom boundary currents in the ocean*, Deep-Sea Res. **22** (1975), 853–873.
33. M.A. Spall and J.F. Price, *Mesoscale variability in Denmark strait: The PV outflow hypothesis*, J. Phys. Oceanogr. **28** (1998), 1598–1623.
34. K. Speer, E. Tziperman and Y. Feliks, *Topography and grounding in a simple bottom layer model*, J. Geophys. Res. **98** (1993), 8547–8558.
35. M.W. Stacey, S. Pond, P. H. LeBlond, H. J. Freeland and D. M. Farmer, *An analysis of the low-frequency fluctuations in the Strait of Georgia, from June 1984 until January 1985*, J. Phys. Oceanogr. **17** (1987), 326–342.
36. M.W. Stacey, S. Pond and P. H. LeBlond, *An objective analysis of the low-frequency currents in the Strait of Georgia*, Atmos.-Ocean **26** (1988), 1–15.
37. ———, *Flow dynamics in the Strait of Georgia, British Columbia*, Atmos.-Ocean **29** (1991), 1–13.
38. G.E. Swaters, *On the baroclinic instability of cold-core coupled density fronts on a sloping continental shelf*, J. Fluid Mech. **224** (1991), 361–382.
39. ———, *Numerical simulations of the baroclinic dynamics of density-driven coupled fronts and eddies on a sloping bottom*, J. Geophys. Res. **103** (1998), 2945–2961.
40. B. Tang and B. Cushman-Roisin, *Two-layer geostrophic dynamics, Part II: Geostrophic turbulence*, J. Phys. Oceanogr. **22** (1992), 128–138.
41. J.A. Whitehead, M.E. Stern, G.R. Flierl and B.A. Klinger, *Experimental observations of baroclinic eddies on a sloping bottom*, J. Geophys. Res. **95** (1990), 9585–9610.

APPLIED MATHEMATICS INSTITUTE, DEPARTMENT OF MATHEMATICAL AND STATISTICAL SCIENCES, UNIVERSITY OF ALBERTA, EDMONTON, ALBERTA, CANADA
E-mail address: mreszka@math.ualberta.ca
url: <http://fluids.math.ualberta.ca/~mreszka/>

APPLIED MATHEMATICS INSTITUTE, DEPARTMENT OF MATHEMATICAL AND STATISTICAL SCIENCES, UNIVERSITY OF ALBERTA, EDMONTON, ALBERTA, CANADA
E-mail address: gordon.swaters@ualberta.ca
url: <http://pacific.math.ualberta.ca/~gordon/>